energies

Article

Comprehensive Numerical Analysis of a Four-Way Two-Position (4/2) High-Frequency Switching Digital Hydraulic Valve Driven by a Ring Stack Actuator

Paolo Tamburrano, Francesco Sciatti *, Elia Distaso and Riccardo Amirante

Department of Mechanics, Mathematics and Management (DMMM), Polytechnic University of Bari, 70121 Bari, Italy; paolo.tamburrano@poliba.it (P.T.); elia.distaso@poliba.it (E.D.); riccardo.amirante@poliba.it (R.A.)
* Correspondence: francesco.sciatti@poliba.it

Abstract: This paper presents a feasibility study using a commercially available ring stack actuator to develop a four way-two position (4/2) high frequency switching digital hydraulic valve. The excellent characteristics of multilayer piezoelectric actuators, such as a simple design, reduced moving parts, high reliability, and fast response, make them ideal for constructing this type of digital hydraulic valve. High frequency switching digital hydraulic valves (HFSVs), indeed, must be able to switch from fully open to fully closed positions in less than 5 ms, while maintaining minimal pressure losses and delivering large flows. The proposed valve architecture is assessed using well-established equations implemented in a Simulink model, allowing the hydraulic, mechanical, and electrical parts of the valve to be accurately simulated. The paper first provides a detailed description of the numerical model. Next, the hysteresis model of the ring stack actuator is validated against the data provided by the manufacturers on their website. Finally, the numerical results obtained with both open-loop and closed-loop control systems are presented. The simulations show that at a switching frequency of 200 Hz with maximum amplitude and duty cycle of the input pulse digital signal, the valve exhibits high average flow rates (~60 L/min), low average power consumption (~1500 W), and maintains a pressure drop of only 15 bar. Moreover, the simulations reveal that the control system is very effective since the valve switching time is within 1 ms.

Keywords: digital hydraulic technology; high frequency switching digital hydraulic valves; simulink

Citation: Tamburrano, P.; Sciatti, F.; Distaso, E.; Amirante, R. Comprehensive Numerical Analysis of a Four-Way Two-Position (4/2) High-Frequency Switching Digital Hydraulic Valve Driven by a Ring Stack Actuator. *Energies* **2023**, *16*, 7355. https://doi.org/10.3390/en16217355

Academic Editors: Inga Konstantinaviciute, Daiva Dumciuviene, Viktorija Bobinaite, Vaclovas Miškinis and Saulius Gudžius

Received: 24 September 2023
Revised: 20 October 2023
Accepted: 25 October 2023
Published: 31 October 2023

1. Introduction

In conventional electro-hydraulic systems, analogue spool valves, including both proportional and servovalves, play a crucial role, as they act as the interface between electric signals and hydraulic power [1,2]. These valves, functioning as directional control valves, regulate the fluid flow directed towards hydraulic actuators in a wide range of applications, including robotics [3], flight simulations [4], gas turbine engines [5], and earthmoving equipment [6]. Despite their notable performance characteristics, such as excellent accuracy [7], precise controllability [8], and rapid response times [9], these valves have been criticized for their susceptibility to impurities and relatively high cost [10,11]. Moreover, proportional and servovalves are known for their significant energy losses, which are mainly attributed to the spool architecture [12]. This design characteristic results in high pressure drops, which in turn lead to elevated power consumption, accounting for 60% of the overall losses in conventional hydraulic systems [13]. In [14], the authors determined, with a simple calculation, that a medium-sized spool valve with a pressure drop of 30 bar and a flow rate of 60 L/min, would dissipate approximately 7 kW of power. Additionally, the energy efficiency of conventional hydraulic systems is significantly influenced by the dynamics of the fluid flow within its various components. The impact of hydrodynamic processes on fluid flow characteristics and their influence on system energy efficiency has recently been explored in [15].

In recent years, there has been a significant increase in interest in the emerging field of digital hydraulic technology. This novel technology aims to enhance the energy efficiency of hydraulic systems through the implementation of digital and discrete control techniques [16–18]. Specifically, these digital and discrete methods are used to actively and intelligently control the output of the system by employing robust and low-cost on/off valves [19]. The remarkable results achieved in various applications, including aircraft brake systems [20], aircraft actuators [21], aircraft fuel systems [22], construction machinery [23,24], conveyors [25], and wave energy recovery systems [26], have demonstrated that digital hydraulic technology has the potential to replace conventional hydraulic technology for the efficient realization of "Industry 4.0" hydraulic systems [27].

The higher energy efficiency of digital hydraulic systems compared to conventional hydraulic systems is attributed to the fact that digital hydraulic valves operate in an on/off manner and may not require a spool for flow adjustment [28]. Consequently, digital hydraulic valves can have the same architecture as that of poppet valves. The poppet valve design, characterized by a larger flow area and absence of leakage, enables efficient control, minimizes energy losses, and thereby improves the performance of the overall hydraulic system [14].

Among the various digital and discrete techniques used to control digital hydraulic valves, pulse width modulation (PWM) stands out as one of the most significant [29,30]. When PWM techniques are employed, digital hydraulic valves are commonly known as high frequency switching digital hydraulic valves (HFSVs) [31].

An HFSV operates by receiving an input pulse digital signal, ranging from 0 to 1, and it enables flow modulation through adjustments of its amplitude and duty cycle. The valve's controllability depends on the switching frequency, with lower frequencies offering better control but increasing pressure pulsation [31].

HFSVs can be used to create a digital hydraulic circuit that replicates the functionality of a conventional four-way three-position (4/3) spool valve. Figure 1 depicts two digital hydraulic circuits of a 4/3 HFSV, where HFSVs are responsible for establishing fluid pathways $P \rightarrow A$, $A \rightarrow T$, $P \rightarrow B$, and $B \rightarrow T$. In particular, in Figure 1a, the digital hydraulic circuit of the 4/3 HFSV is realized using four two-way two-position (2/2) HFSVs. However, to reduce the number of components, the digital hydraulic circuit of the 4/3 HFSV can be obtained with just two four-way two-position (4/2) HFSVs, as depicted in Figure 1b.

The HFSVs utilized in the digital hydraulic circuits presented in Figure 1 are designed to meet specific requirements. These include the need to switch rapidly from fully open to closed positions in less than 5 ms, with minimal pressure losses, and the capacity to provide high flow rates while maintaining a compact design [14]. To achieve high switching speeds, smart materials like piezoelectric actuators, with their simple design, few moving parts, high reliability, and rapid response times, are well suited for constructing this type of digital hydraulic valve [32].

Over the years, remarkable advancements have been made in the development of HFSVs driven by piezoelectric actuators. In 1991, Yokota et al. developed a 2/2 HFSV with the use of two piezoelectric actuators, achieving an impressive 0.1 ms switching time and a flow rate of 7.2 L/min at 100 bar [33,34]. In 2000, Yamada et al. realized a 2/2 HFSV with a spring mechanism and a piezo stack actuator, obtaining a switching time less than 0.8 ms and a flow rate of 3 L/min at 100 bar [35]. In 2008, Ouyang et al. utilized three piezo stack actuators in a 2/2 HFSV, resulting in a switching time of less than 1 ms and a flow rate of 10 L/min at 200 bar [36]. In 2019, Yu et al. realized a 2/2 HFSV using a piezo stack actuator with a diamond mechanism amplification, reaching a switching time less than 1 ms and a flow rate of 17.4 L/min at 150 bar [37].

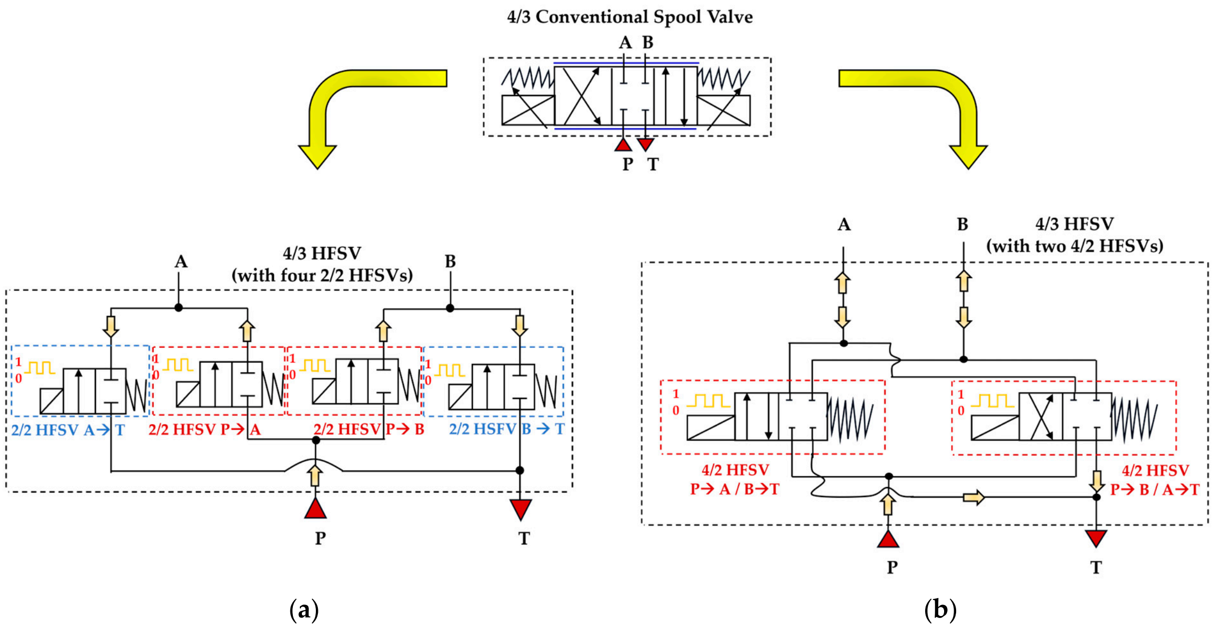

Figure 1. Digital version of a conventional 4/3 Spool Valve: (**a**) 4/3 HFSV made up of four 2/2 HFSVs; (**b**) 4/3 HFSV made up of two 4/2 HFSVs.

Despite the fast-switching times, all the "piezo 2/2 HFSVs" discussed earlier cannot be employed in the digital hydraulic circuit depicted in Figure 1a, as a replacement for a conventional spool valve, due to their limited flow rate delivery. To address this limitation, the authors of this paper conducted a feasibility study on a novel and innovative 2/2 HFSV architecture [14]. This valve utilizes a multilayer piezoelectric actuator, known as the ring stack, for its actuation. Through open loop predictions performed within the Simulink environment, it was demonstrated that this valve can be effectively integrated into the 4/3 HFSV digital hydraulic circuit shown in Figure 1a, serving as a viable alternative to proportional and servovalves in various high-speed control applications.

In this scenario, with the aim of simplifying the digital hydraulic circuit from the 4/3 HFSV configuration shown in Figure 1a to that presented in Figure 1b, and with the goal of improving the energy efficiency of hydraulic systems, the purpose of this study is to investigate a novel 4/2 HFSV architecture based on the use of the same ring stack actuator. Specifically, building upon our 2/2 HFSV Simulink model [14], the paper proposes an enhanced numerical code that allows for the simulation of open loop step tests, assessment of the hysteresis of the piezoelectric actuator, and execution of closed loop step tests, offering a more comprehensive analysis.

The paper starts with a detailed description of the valve architecture, illustrating the flow of the equations that are utilized in the Simulink model to evaluate the valve's performance. This is followed by the validation of the hysteresis model of the ring stack actuator, where a comparison is made between the simulated and real curve in terms of percentage error, based on data from the manufacturer's website. Subsequently, the paper presents and discusses the numerical results obtained with both open-loop and closed-loop control systems. The results provide insights into the advantages and disadvantages of the proposed valve architecture, which are further discussed in the conclusions.

2. Valve Architecture

To create a novel 4/2 HFSV that can be integrated into the digital hydraulic circuit illustrated in Figure 1b, it is necessary to fulfil the following requirements:

✓ Rapid Switching Time: The valve must be capable of switching between open and closed positions within a very short time interval, specifically less than 5 milliseconds;

✓ Low Pressure Drops: Even at high flow rates, the valve must generate minimal pressure drops in order to prevent energy dissipation. The desired target is to achieve a maximum pressure drop of 15 bar at a flow rate of 60 L/min;

✓ Robustness: The valve must be robust and reliable and capable of handling numerous operational cycles without compromising its functionality or durability.

To achieve the specified goals, a ring stack actuator is used to actuate the valve. These actuators are composed of multiple layers, with thicknesses typically ranging from 50 to 100 µm. This design allows them to generate considerable actuation forces by utilizing high electrical fields (2–3 kV/mm) while operating at a low voltage of around 200 V [38]. Additionally, the height of the stack of these actuators determines the combination of two important factors, namely the free stroke and the blocking force. The former represents the ideal maximum displacement that can be obtained when no resistant forces are present, and the maximum operating voltage is applied. The latter represents the maximum actuation force that can be provided when the actuator is prevented from moving with the maximum operating voltage applied.

The specific ring stack actuator chosen for this purpose is manufactured by Noliac, namely the model NAC2125-HXX with the maximum height (H = 200 mm) [39]. It is capable of producing the highest value of maximum free stroke (x_{max}= 325 µm). The maximum blocking force of this actuator is $F_{b,max}$= 8450 N, while its stiffness is k_p= 26 N/µm. The detailed specifications are outlined in Table 1 [39].

Table 1. NAC2125-HXX Ring Stack: Specifications [39].

Parameter	Symbol	Value	Unit
Outer Diameter	D	20	mm
Inner Diameter	d	12	mm
Height	H	200	mm
Max. Operating Voltage	V_{max}	200	V
Max. Blocking Force	$F_{b,max}$	8450	N
Max. Free Stroke	x_{max}	325	µm
Capacitance	Cap	79,300	nF
Stiffness	k_p	26	N/µm

The operation of the proposed 4/2 HFSV architecture is illustrated in Figure 2. In this design, the valve remains closed thanks to contact between the poppets (2) and the valve seats (5). To initiate valve opening, a digital signal is transmitted to activate the ring stack actuator (1). Consequently, the poppets, which are inserted through the hole of the stack (3), move downward, disengaging from their respective valve seats and allowing the valve to open. Additionally, the design includes a spring (4) with the dual function of maintaining close contact between the poppets and the piezoelectric actuator and ensuring the correct pre-compression of the latter. This pre-compression is necessary because piezo stack actuators cannot handle large pulling forces, and applying a preload helps prevent damage. It has been widely demonstrated that using the correct preload value significantly extends the lifetime of this type of piezoelectric actuator [40]. Specifically, the optimal preload values typically fall within the range of 20 to 50 percent of the blocking force [41].

As mentioned earlier, when no voltage is applied to the ring stack actuator, no deformation occurs, and as a result, the valve remains closed, as depicted in Figure 2a. However, when a differential voltage is applied to the ring stack actuator, the poppets move from their original positions, leading to the opening of the valve. Consequently, oil flow is permitted from Port P to Port A, and from Port B to Port T, as illustrated in Figure 2b.

One critical aspect of HFSVs pertains to their frequent daily switching requirements. As a result, they must exhibit high resistance to wear and fatigue. In the selected 4/2 HFSV design, the poppets and their respective valve seats assume an important role in fulfilling these requirements. Any mismatch between these components could lead to adverse effects on sealing and the overall lifespan of the valve. To address this challenge, stainless steel is selected for the poppets, while nickel aluminum bronze is chosen for the valve seats, in line with recommendations provided by poppet valve manufacturers [42].

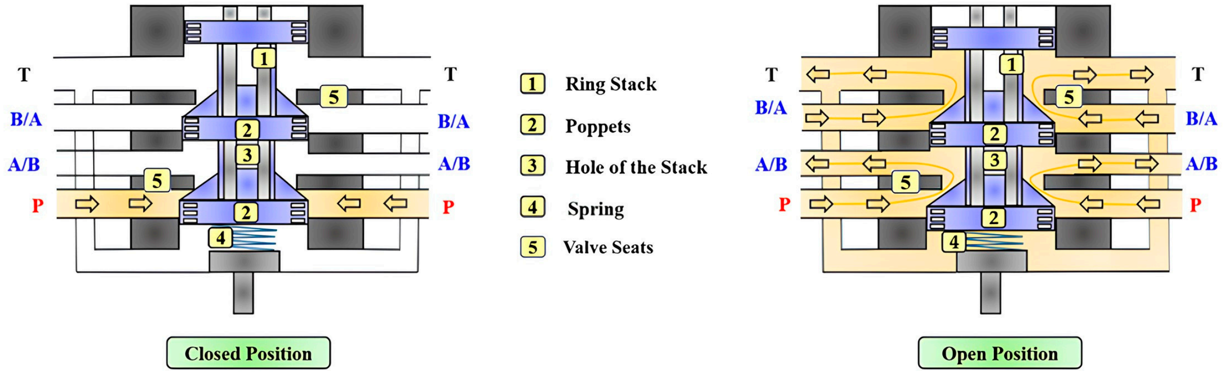

(**a**) (**b**)

Figure 2. Proposed 4/2 HFSV architecture: Closed Position (**a**); Open Position (**b**).

3. Numerical Model of the 4/2 HFSV Actuated by a Ring Stack

The evaluation of the suggested valve architecture's performance, specifically the one illustrated in Figure 2, is conducted by using well-established and referenced equations integrated within Simulink, leveraging the Simscape Fluids libraries [43]. This approach ensures the validation of the hydraulic model. Additionally, since this model is an extension of our previously verified code [14], its validation is assured.

The equations implemented in Simulink are described in the following, referring to the actuation of the ring stack and the resulting opening of the valve, as shown in Figure 3.

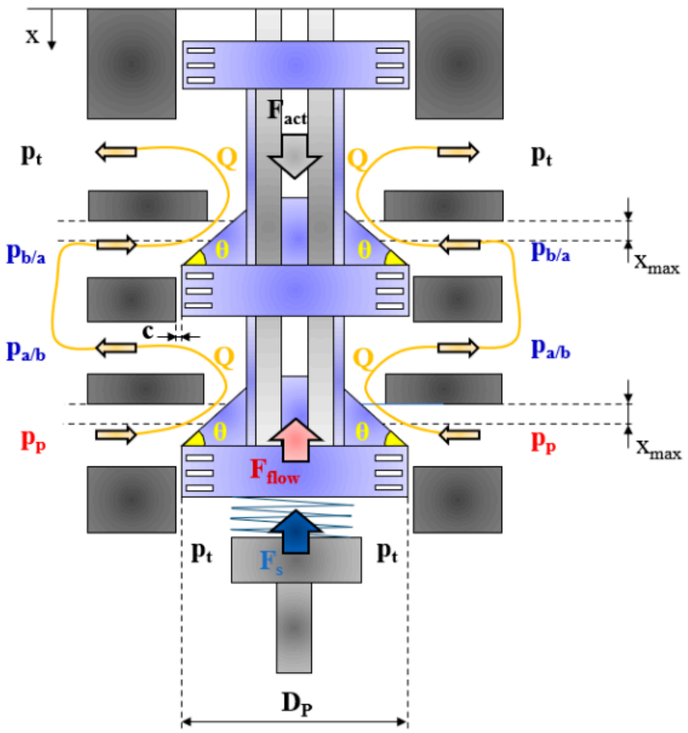

Figure 3. Illustration of the modeled valve architecture in the open position, featuring the key system parameters employed and the main output variables obtained (please note that the radial clearance, denoted as "c", has been overestimated for clarity).

The ring stack necessitates an amplifier, which is responsible for converting a low-input control voltage, characterized by an overall period (τ), a switching frequency (f), an amplitude (V_c), and a duty cycle (DC), into a high-output voltage (V_{amp}). The relation between the output and the input voltage is simulated by using a second order transfer function G(s) [14]:

$$G(s) = \frac{V_{amp}}{V_c} = \frac{k_a \omega_n^2}{s^2 + 2\xi\omega_n s + \omega_n^2}, \quad (1)$$

where s is the complex variable, while k_a, ω_n, and ξ are the gain, natural frequency and damping ratio of the amplifier, respectively. The current limit of the amplifier, I_{max}, is computed as follows [14]:

$$\left(\frac{dV_{amp}}{dt}\right)_{max} = \frac{I_{max}}{C_{ap}}, \quad (2)$$

where C_{ap} is the capacitance of the ring-stack.

The consideration of piezoelectric hysteresis involves the implementation of the Bouc–Wen hysteresis model, as described and used in reference [44]. This model enables the computation of the hysteresis nonlinear term, n:

$$\frac{dn}{dt} = \alpha\frac{dV_{amp}}{dt} - \beta\left|\frac{dV_{amp}}{dt}\right|n - \delta\frac{dV_{amp}}{dt}|n|, \quad (3)$$

where α, β and δ are parameters to be adjusted in order to adapt the hysteresis model to a specific case. The hysteresis non-linear term, n, is used to correct the blocking force, F_b, because of hysteresis, as follows [44]:

$$F_b = K_b K_{VF}\left(V_{amp} - n\right), \quad (4)$$

where K_b is a correction factor, to be tuned in order to match the numerical model with the experimental data provided by the manufacturer; whereas K_{VF} is a conversion factor (from voltage to force).

The blocking force, F_b, determines the actuation force, F_{act}, which can be calculated as follows [14]:

$$F_{act} = F_b - k_p x, \quad (5)$$

where k_p and x are the stiffness and the displacement of the actuator (the latter is equal to the poppets' displacement).

When the valve is actuated, the equilibrium of the forces acting on the poppets can be expressed as:

$$F_{act} - F_s - F_{flow} - F_c - F_i = 0, \quad (6)$$

where:

- F_s is the force of the additional spring given by $F_s = k_s\,(x + \delta_0)$, with k_s and δ_0 representing the stiffness and the pre-compression of the additional spring;
- F_c is the force of the additional spring given by $F_c = C\dot{x}$, with C representing the damping factor of the poppets (accounting for fluid viscosity);
- F_i is the inertia force given by $F_i = m\ddot{x}$, with m representing the mass of the moving parts.
- F_{flow} represents the flow forces acting on the poppets.

To determine the damping factor of the poppets, C, which accounts for the frictional forces acting on them, the following relationship can be utilized [14]:

$$C = \frac{\mu\pi D_p l_p}{c\sqrt{1 - \left(\frac{\varepsilon}{c}\right)^2}}, \quad (7)$$

where μ is the dynamic viscosity of the oil, D_p and l_p are the poppets' diameter and length of the part in contact with the case; c is the radial clearance and ε is the radial eccentricity.

The flow of fluid through the valve ports leads to the generation of steady-state and transient flow forces. Steady-state flow forces, which are hydrodynamic effects in stable flow conditions, can be further categorized as axial and radial flow forces [45]. In contrast, transient flow forces are instantaneous hydrodynamic phenomena that occur during sudden valve port opening or closing [46]. This analysis focuses only on steady-state flow forces, which occur as oil flows through the two metering chambers. The evaluation of these forces can be performed using the following equation [44,47]:

$$F_{flow} = 2\rho \frac{Q^2}{A_r} \cos\vartheta, \tag{8}$$

where the factor 2 considers the two metering chambers being opened simultaneously, ρ is the oil density, and ϑ is the velocity angle with respect to the horizontal direction; the volumetric flow rate, Q, and the restriction area, A_r, through each metering chamber can be calculated by the following equations [14]:

$$A_r = \pi D_p x \sin\vartheta, \tag{9}$$

$$Q = C_D A_r \sqrt{\frac{\Delta p}{\rho}}, \tag{10}$$

where C_D is the discharge coefficient and Δp is the overall pressure drop across the valve. In the model, Port A and Port B are hydraulically connected, and the pressure drop is neglected. Therefore, the pressure drop in Equation (9) becomes:

$$\Delta p = p_P - p_T = 2(p_B - p_T) = 2(p_P - p_A), \tag{11}$$

When oil flows through the metering chambers, it experiences a pressure drop, which results in power consumption. The ideal power average loss in the 4/2 HFSV, $P_{d,v}$ can be determined as follows [47]:

$$P_{d,v} = Q_M \Delta p, \tag{12}$$

where Q_M is the average flow rate provided by the valve.

The range of motion for the poppets is constrained by two stops, defining the upper and lower bounds. Each stop incorporates a combination of a spring and a damper. When the poppets reach their maximum displacement ($x = x_{max}$) or minimum displacement ($x = x_{min} = 0$), a force (F_{stop}) is exerted on the ring stack. The calculation for this force is evaluated as follows [14]:

$$\begin{gathered} F_{stop} = K_{stop}(x_{max} - x) + C_{stop}\frac{d}{dt}(x_{max} - x), \\ \text{for} \quad x \geq x_{max} \end{gathered} \tag{13}$$

$$\begin{gathered} F_{stop} = K_{stop}(x_{min} - x) + C_{stop}\frac{d}{dt}(x_{min} - x), \\ \text{for} \quad x \leq 0 \end{gathered} \tag{14}$$

To simulate the volume of oil between ports (P) and (A), as well as between ports (B) and (T), a block named "Constant Volume Hydraulic Chamber" is utilized. This block serves the purpose of mimicking a chamber with fixed volume and rigid walls, while also considering the compressibility of the fluid. The following equations are applied [14]:

$$V_{cham} = V_0 + \frac{V_0 p}{E}, \tag{15}$$

$$q_c = \frac{dV_{cham}}{dt} = \frac{V_0}{E}\frac{dp}{dt}, \tag{16}$$

where V_0 represents the geometrical volume of the chamber. This value is obtained by multiplying the internal diameter (D_0) by the overall internal length (L_0). On the other hand, V_{cham} represents the volume of oil in the chamber at a given pressure (p), while

q_c represents the volumetric flow rate through the chamber. To calculate the actual bulk modulus (E), the following equation is used [14]:

$$E = E_0 \frac{1+\sigma\left(\frac{p_a}{p}\right)^{1/\gamma}}{1+\sigma\frac{p_a{}^{1/\gamma}}{\gamma\, p^{(\gamma+1)/\gamma}}E_o}, \tag{17}$$

Both open and closed-loop control systems can be simulated. In the former control system, users have the flexibility to set the switching frequency (f), the overall period (τ), the duty cycle (DC), the amplitude (V_c) of the input control voltage, as well as the overall pressure across the valve (Δp). The resulting output variables include the average flow rate (Q_M) and the average power consumption ($P_{d,v}$). Conversely, in the latter control system, a Proportional-Integral (PI) controller is employed to adjust the duty cycle of the input pulse digital signal, aiming to achieve the desired average flow rate, based on the calculated error term e(t):

$$DC = K_P e(t) + K_I \int_0^t e(t)dt \tag{18}$$

where K_P and K_I denote the proportional and integral gain, respectively. The controller does not incorporate derivative action due to its susceptibility to noise in the process-variable signal.

The Simulink solver, specifically Ode14x, calculates the states of the dynamic system at consecutive time intervals of 0.1 ms over a defined period.

To recap, Figures 4 and 5 display two structured block diagrams that provide a visual representation of how the previously described equations flow in open and closed control systems, respectively. The color of each block clarifies whether it represents the input variables, the input system parameters, or the resulting output variables.

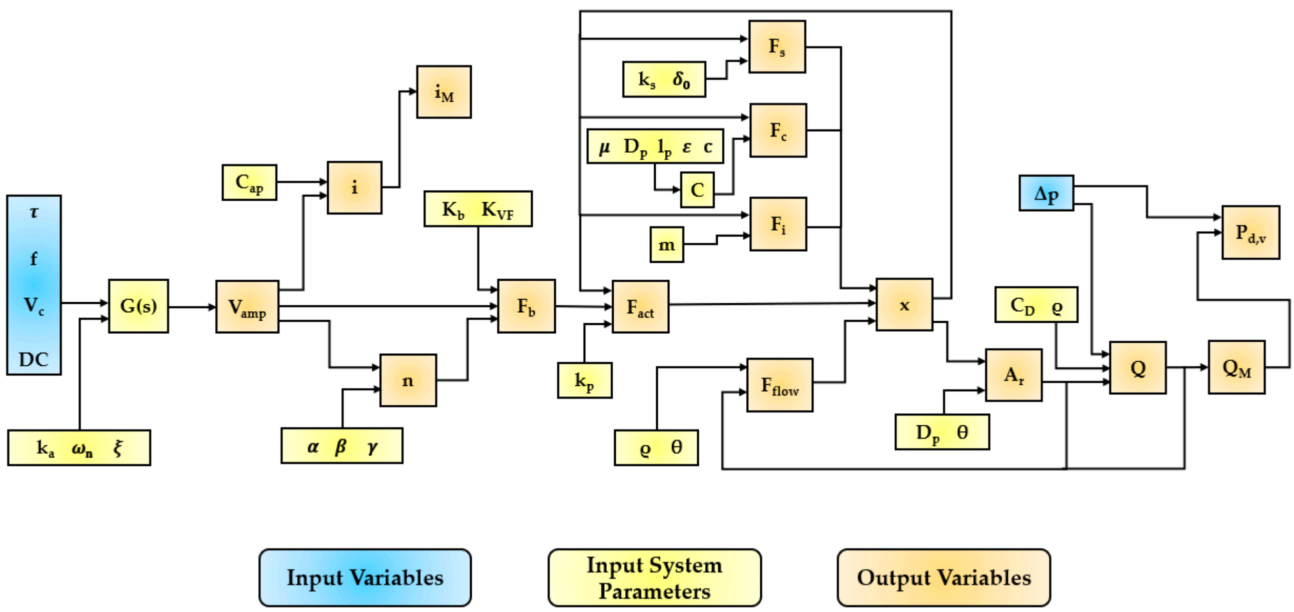

Figure 4. Equation Flow in the Open-Loop Control System: Input Variables, Input System Parameters, and Output Variables.

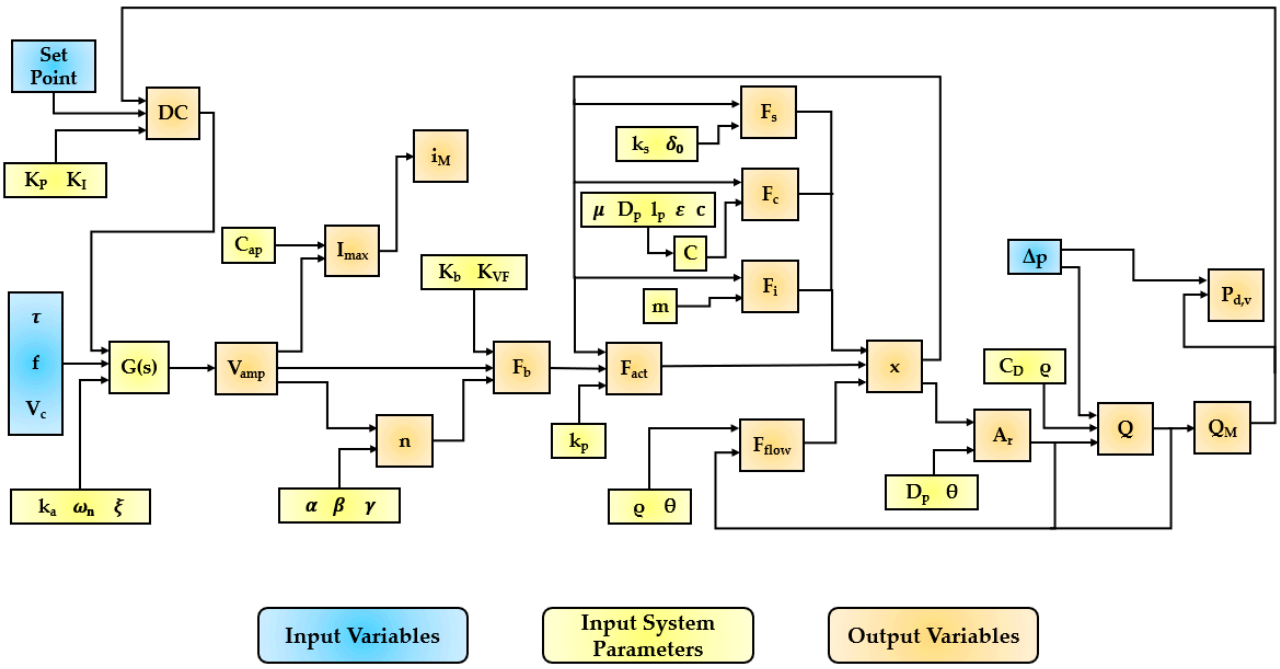

Figure 5. Equation Flow in the Closed-Loop Control System: Input Variables, Input System Parameters, and Output Variables.

4. Results

The following section presents and discusses the results of the numerical simulations conducted on both metering chambers of the 4/2 HFSV, specifically P → A and B → T. The initial step involved the validation of the hysteresis model using the data provided by Noliac on their website [39]. Figure 6 visually represents the hysteresis curve, illustrating the relationship between the electric field supplied to the actuator and the resulting strain percentage. More precisely, Figure 6a,b illustrates the percentage error between the ascending and descending branches obtained by the simulation and provided by the manufacturer, respectively. Meanwhile, Figure 6c offers a comprehensive comparison of the entire simulated hysteresis curve with the corresponding manufacturer's data. The manufacturer's curve pertains specifically to the piezoceramic material NCE51F, which is used in constructing the NAC 2125 HXX ring stack model. It is important to note that the strain percentage indicated on the graph applies exclusively to the active material. In practical multilayer piezoelectric actuators, there are additional inactive layers present on each ceramic element, as well as on the top and bottom of the entire stack. Considering a total stack height of 200 mm, the active material accounts for a length of 156 mm, with each active layer in the stack having a thickness of around 67 µm. In the graph, the hysteresis curve plotted in red with a continuous line represents the manufacturer's data. To obtain the simulated hysteresis curve (plotted in blue with a dotted line), the mentioned equations in Section 3 were used with tuned parameters $\alpha = 0.53$, $\beta = 0.009$, $\delta = 0.02$ and $K_b = 1.09$. A 1 Hz sinusoidal input control voltage with amplitude, ranging from 0 to +5 V, was applied in the simulation. No load was applied, meaning F_{flow}, F_s, F_c, F_i and Q were all set to 0. The simulation utilized the characteristics of the NAC2125 H200 model, where $F_{b,max} = 8450$ N and $k_p = 26$ N/µm. The amplifier employed in the simulations is characterized by $\omega_n = 10{,}000$ rad/s, $k_a = 40$ and $\xi = 1.5$. The close agreement between the simulation curve and the manufacturer's curve, with a percentage error of less than 15% in both the ascending and descending branches, demonstrates the accuracy of the hysteresis model.

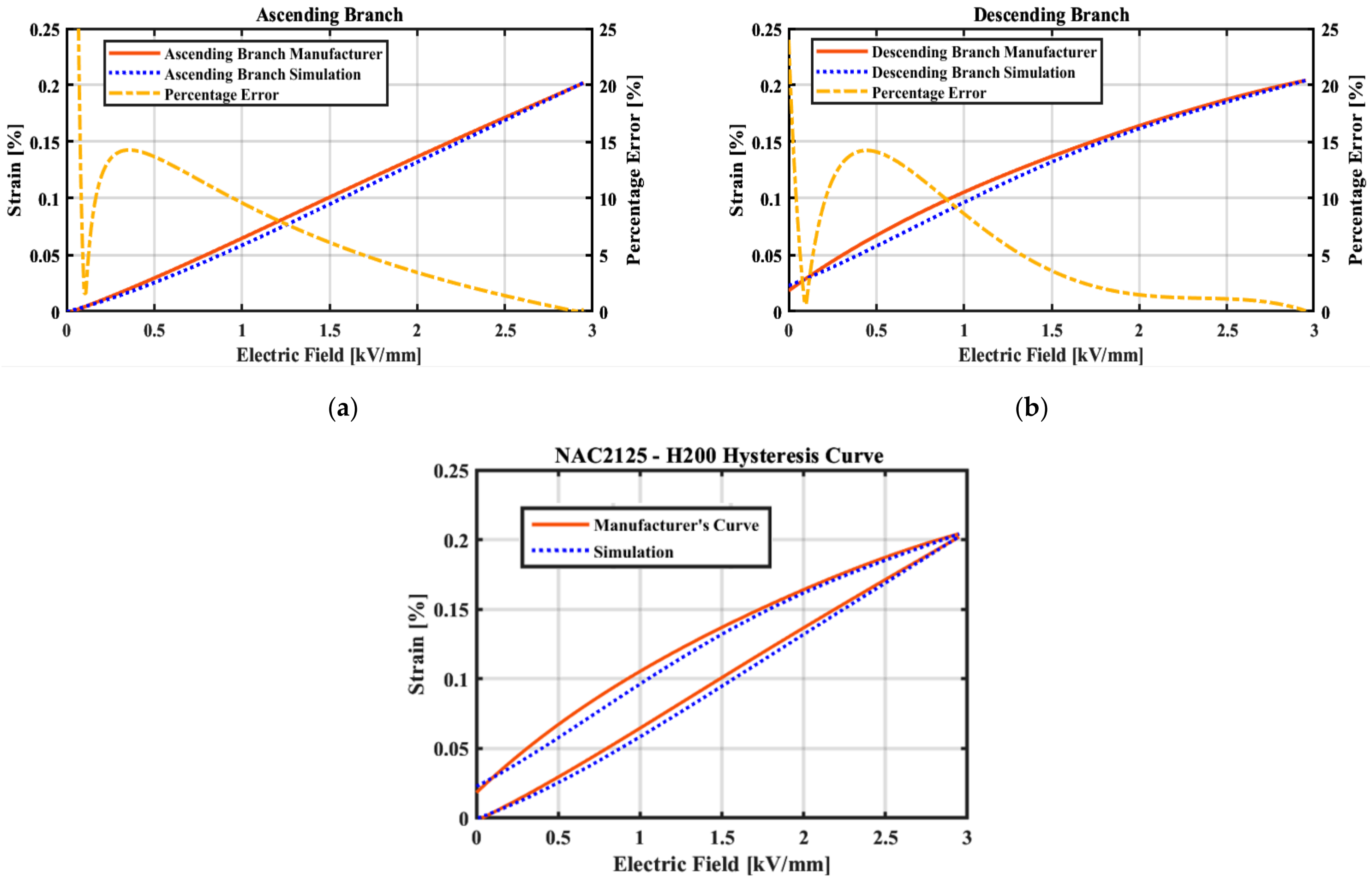

(**a**) (**b**) (**c**)

Figure 6. Hysteresis curve provided by the manufacturer compared with the hysteresis curve obtained from the simulations: (**a**) Ascending Branch; (**b**) Descending Branch; (**c**) Entire Hysteresis Curve.

Once the hysteresis model was validated, the 4/2 HFSV architecture depicted in Figure 4 was simulated using the numerical code described in Section 3.

In the simulation, the oil used was ISO VG 32, maintained at a temperature of 50 °C. The oil properties were characterized by a density $\rho = 851\ \mathrm{kg/m^3}$ and $\mu = 0.0187\ \mathrm{kg/(ms)}$. The discharge pressure to the tank (p_t) was assumed to be constant and equal to 1 bar. Considering the dimensions of the ring stack actuator, the two poppets inserted through the hole of the stack were assumed to have a diameter $D_p = 60$ mm and an angle $\theta = 45°$. For the same reason, the length of the part in contact with the case (l_p) was assumed to be 50 mm, with a clearance (c) of 1 µm. Taking the piezoelectric actuation into an account, a mass m = 100 g was considered to represent the moving parts. The damping factor of the poppets was calculated using Equation (7): assuming negligible eccentricity (ε), the calculated damping factor is C = 60 Ns/m. The chamber accounting for fluid compressibility, given the dimensions of the poppets, was assumed to have $D_0 = D_p = 60$ mm and $L_0 = l_p = 50$ mm, thus obtaining $V_0 = 2 \times 10^{-4}\ \mathrm{m^3}$. Regarding the discharge coefficient, it was assumed to remain constant at $C_D = 0.7$, under the hypothesis of turbulent flow [1].

To achieve a preload equal to 20% of the maximum blocking force [25], the additional spring was assumed to have a stiffness of $k_s = 190{,}000$ N/m. It was pre-compressed by $\delta_0 = 8.90$ mm. The maximum displacement, represented by the mechanical stop, was defined as $x_{max} = 0.325$ mm, which corresponds to the maximum free stroke of the ring stack. For the mechanical stops, the spring stiffness was set to $K_{stop} = 10^7$ N/m, while the damping was assigned a value of $C_{stop} = 3000$ Ns/m.

The operating parameters for the ring stack actuator were reported in Table 1, while the input system parameters, including the hysteresis parameters for the ring stack, can be found in Table 2. Additionally, Table 3 shows the input and output variables that will be set and obtained from the simulations for both open and closed-loop control systems.

Table 2. Simulated Input System Parameters and Nomenclature.

Component	Parameter	Symbol	Value	Unit
Oil (ISO VG 32)	Temperature	T	50	°C
	Density	ρ	851	kg/m^3
	Viscosity	μ	0.0187	kg/(ms)
Discharge Line	Discharge Pressure	p_t	1	bar
Amplifier	Natural Frequency	ω_n	10,000	rad/s
	Gain	k_a	40	-
	Damping Ratio	ξ	1.5	-
Ring Stack	Hysteresis Parameter	α	0.53	-
	Hysteresis Parameter	β	0.009	-
	Hysteresis Parameter	δ	0.02	-
	Hysteresis Parameter	K_b	1.09	-
4/2 HFSV	Conversion factor K_{VF}	K_{VF}	42.25	N/V
	Mass Moving Parts	m	100	g
	Poppets' Diameter	D_p	60	mm
	Length Parts Contact Case	l_p	50	mm
	Clearance	c	1	µm
	Eccentricity	ε	0	µm
	Poppets' Damping Factor	C	60	Ns/m
	Poppets' Angle	θ	45	°
	Chamber Volume	V_{cham}	2×10^{-4}	m^3
	Discharge Coefficient	C_D	0.7	-
	Stiffness Additional Spring	k_s	190,000	N/m
	Pre-compression	δ_0	8.9	mm
	Spring stiffness Stop	K_{stop}	107	N/m
	Damping Factor Stop	C_{stop}	5000	Ns/m

Table 3. Input and Output Variables Nomenclature for both Open and Closed-Loop Control Systems.

Variables	Open Loop	Closed Loop	Symbol	Unit
Overall Period	Input	Input	τ	ms
Switching Frequency	Input	Input	f	Hz
Amplitude	Input	Input	V_c	V
Duty Cycle	Input	Output	DC	-
Overall Pressure Drop	Input	Input	Δp	bar
Set Point	-	Input	Set Point	L/min
Amplified Voltage	Output	Output	V_{amp}	V
Current	Output	Output	i	A
Average Current	Output	Output	i_M	A
Hysteresis Term	Output	Output	n	V
Blocking Force	Output	Output	F_b	N
Actuation Force	Output	Output	F_{act}	N
Inertia Force	Output	Output	F_i	N
Viscous Force	Output	Output	F_c	N
Add. Spring Force	Output	Output	F_s	N
Flow Force	Output	Output	F_{flow}	N
Poppets' Position	Output	Output	x	µm
Flow Rate	Output	Output	Q	L/min
Average Flow Rate	Output	Output	Q_M	L/min
Average Power Con.	Output	Output	$P_{d,v}$	W

All the numerical results were obtained by maintaining the period of the input pulse digital signal constant (or input control voltage) constant, specifically set at τ = 5 ms, resulting in a switching frequency equal to f = 200 Hz.

First, the impact of the amplitude of the input control voltage on the performance of the 4/2 HFSV was investigated. Figure 7 shows open-loop predictions conducted with varying amplitudes of the input pulse digital signal during four different periods: 0 to 2 V, 0 to 3 V, 0 to 4 V, and 0 to 5 V. The analysis took into account an overall pressure drop across the valve of $\Delta p = 15$ bar and a duty cycle of the input pulse digital signal set at DC = 60%. Specifically, Figure 7a shows the time history of the quantities provided to the ring stack actuator. These quantities include the amplitude of the input control voltage, V_c (multiplied by 20 for clarity), the amplified voltage, V_{amp}, the current, i, and the average current, i_M. Furthermore, the time history of the resulting blocking force achieved, F_b, is also depicted in the graph. Figure 7b illustrates the time history of the forces related to the actuation of the ring stack. Specifically, it presents the actuation force developed by the ring stack, denoted as F_{act}, along with the resistant forces. These resistant forces included the viscous force, F_c, the inertia force, F_i, the force of the additional spring, F_s, and the flow forces, F_{flow}. Figure 7c displays the time history of poppets' position, x, the obtained instantaneous flow rate, Q, the obtained average flow rate, Q_M, and the average ideal power dissipated by the valve, $P_{d,v}$.

Referring to Figure 7a, the amplitude of input control voltage, V_c, is amplified to a higher pulse voltage, V_{amp}, by the amplifier within approximately 1 ms. This amplified voltage was then corrected by the hysteresis non-linear term, n, and then converted into the blocking force, F_b, using the conversion factor, K_{VF}, and the correction factor, K_b. It is worth noting that a higher amplitude of the input control voltage resulted in a higher blocking force. Specifically, when the amplitude of the input control voltage reached its maximum value of 5 V, the maximum value of the blocking force was obtained. However, due to the hysteresis of the ring stack actuator, the blocking force did not return to zero when the input control voltage was removed. Moreover, the graph revealed that as the amplitude of the input control voltage increased, the current, i, experienced a higher peak value. In particular, during the fourth period, the peak of current reached its maximum value of 43.5 A. However, it is important to note that this peak of current occurred only for a short duration, and the average current, i_M, remained relatively low, below 6 A.

When examining the predictions of Figure 7b, it became apparent that both the viscous force, F_c, and the flow force, F_{flow}, had negligible effects on the actuation capability of the ring stack actuator. This was because these forces were considerably smaller than the actuation force, F_{act}, which was determined by the difference between the blocking force, F_b, and the ring stack spring force, $k_p x$. Therefore, the actuation force did not return to zero when the input control voltage was removed. On the other hand, the force of the additional spring, F_s, and the inertia force, F_i, played significant roles in the actuation of the ring stack. The force of the additional spring was particularly influential due to the value of the preload, δ_0. On the other hand, the oscillations in the actuation force were caused by the inertia force attributed to the relatively lower damping factor, C, calculated for the poppets. Therefore, it was crucial to ensure that the mass of the moving parts, m, was not excessively large in order to minimize these oscillations and enhance the performance of the 4/2 HFSV.

With regard to the predictions of Figure 7c, the actuation force, F_{act}, allowed the poppets to move and reach the open position in less than 1 ms. Due to the oscillations in the actuation force, the poppets oscillated around the open position, which may not have been equal to the maximum free stroke, x_{max}, due to the presence of resistant forces. However, despite the hysteresis of the ring stack actuator, the force stored in the additional spring, F_s, was substantial enough to ensure that the poppets could close the valve when the input control voltage was removed. The poppets' position, x, exhibited a similar trend to the obtained instantaneous flow rate, Q, indicating a correlation between the two variables. It is worth noting that the amplitude of the input control voltage, V_c, directly influenced the obtained average flow rate, Q_M. As the amplitude increased, the average flow rate also increased. During the fourth period, when the amplitude of the input control voltage reached its maximum value (i.e., $V_c = 5$ V), an average flow rate of $Q_M = 34.74$ L/min was achieved. Given that the overall pressure drop across the valve remained constant, the ideal average power dissipated by the valve, $P_{d,v}$, followed a similar trend to the average flow rate. It is important to note that when the input control voltage was equal to its maximum, an ideal average power consumption of only $P_{d,v}$ =868.4 W was observed.

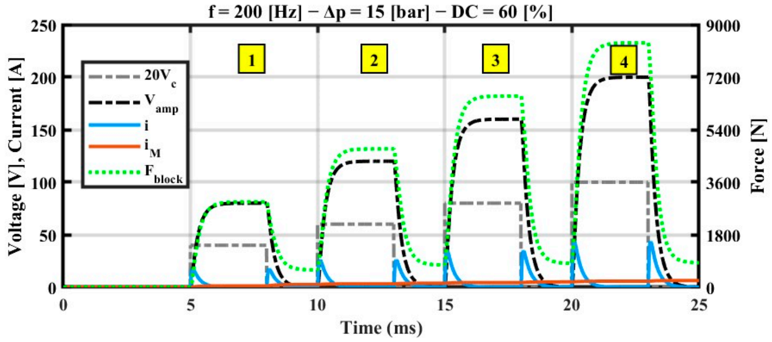

(**a**)

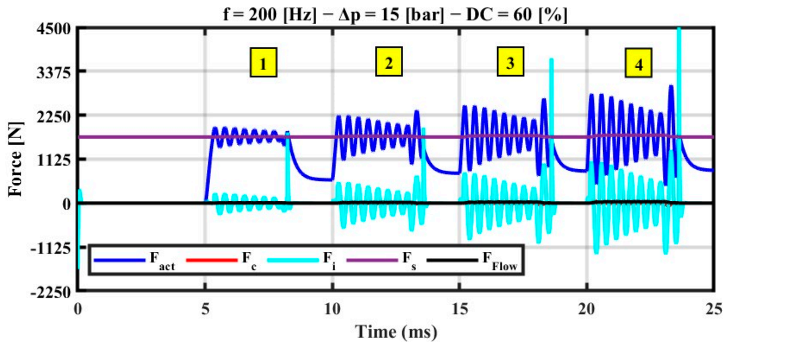

(**b**)

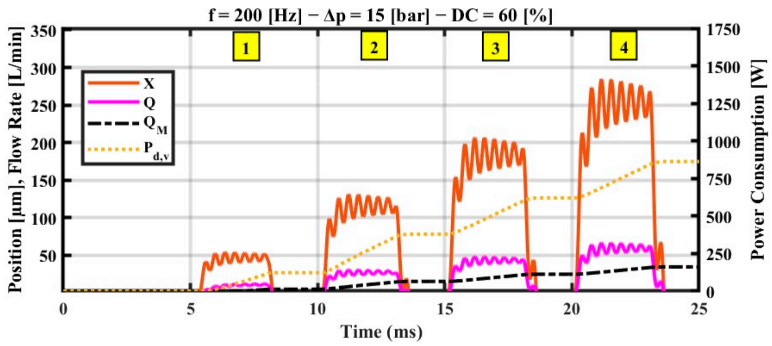

(**c**)

Figure 7. Open-loop predictions simulated for four different values of V_c (1: 0 to 2 V; 2: 0 to 3 V, 3: 0 to 4 V; 4: 0 to 5 V) with f = 200 Hz, Δp = 15 bar and DC = 60%: (**a**) Amplitude of the Input Control Voltage, Amplified Voltage, Current, Average Current, Blocking Force; (**b**) Actuation Force, Viscous Force, Inertia Force, Additional Spring Force, Flow Force; (**c**) Poppets' Position, Flow Rate, Average Flow Rate, Ideal Average Power Dissipated by the Valve.

The results shown in Figure 8 provide an evaluation of how the performance of the 4/2 HFSV is affected by the duty cycle of the input control voltage. To conduct these evaluations, open-loop step tests were performed, resembling the tests shown in Figure 7, but this time changing the duty cycle of the input pulse digital signal. Four different periods, with different values of the duty cycle, were examined, specifically DC = 30%, DC = 40%, DC = 60%, and DC = 80%. The analysis considered an overall pressure drop across the valve of $\Delta p = 15$ bar and an amplitude of the input control voltage of $V_c = 5$ V. It is evident that increasing the duty cycle, DC, led to a higher average flow rate, Q_M, and, consequently, an increase in the ideal average power dissipated by the valve, $P_{d,v}$. Specifically, during the fourth period with a duty cycle of 80%, an average flow rate of $Q_M = 46.78$ L/min and an ideal average power consumption of $P_{d,v} = 1170$ W were achieved.

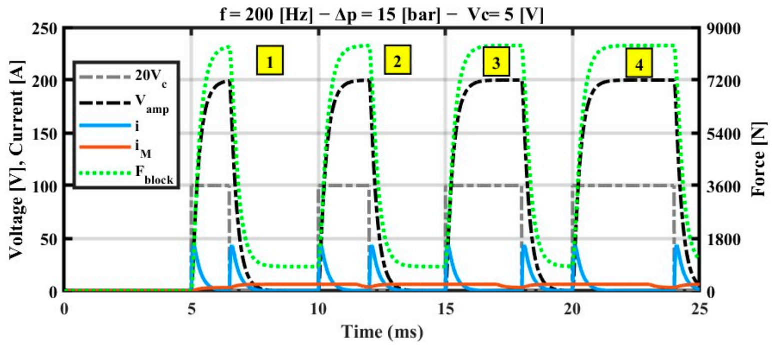

(**a**)

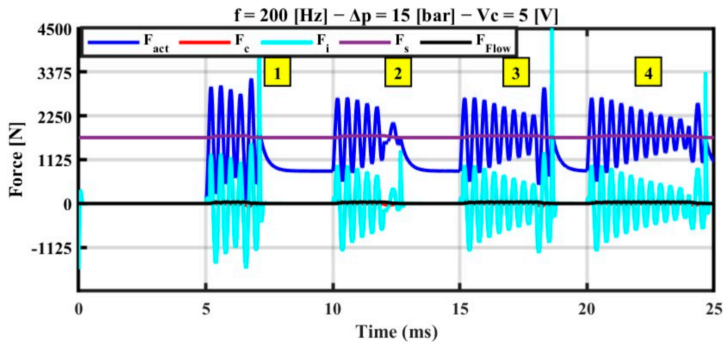

(**b**)

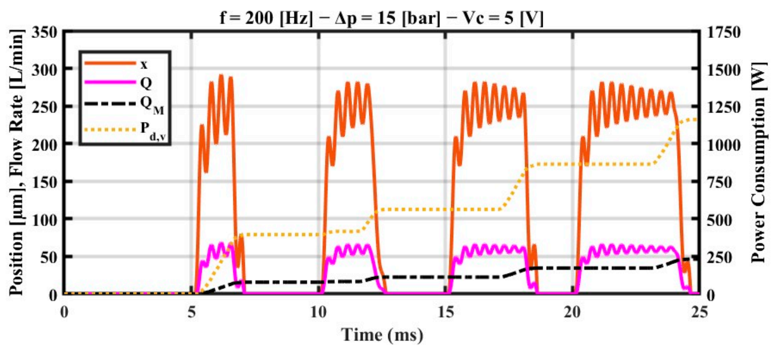

(**c**)

Figure 8. Open-loop predictions simulated for four different values of DC (1: 30%; 2: 40%; 3: 60%; 4: 80%) with f = 200Hz, $\Delta p = 15$ bar, $V_c = 5$ V: (**a**) Amplitude of the Input Control Voltage, Amplified Voltage, Current, Average Current, Blocking Force; (**b**) Actuation Force, Viscous Force, Inertia Force, Additional Spring Force, Flow Force; (**c**) Poppets' Position, Flow Rate, Average Flow Rate, Ideal Average Power Dissipated by the Valve.

To resume the impact of the amplitude (V_c) and duty cycle (DC) of the input control voltage, Figure 9 illustrates the average flow rate (Q_M) provided by the valve as the amplitude and duty cycle of the input control voltage vary. The analysis considered an overall pressure drop across the valve of Δp =15 bar. The simulations demonstrated that as both the amplitude and duty cycle of the input control voltage increased, the average flow rate also increased. Specifically, when applying the maximum duty cycle and maximum amplitude of the input control voltage to the ring stack actuator, the valve achieved an impressive average flow rate of $Q_M = 60$ L/min.

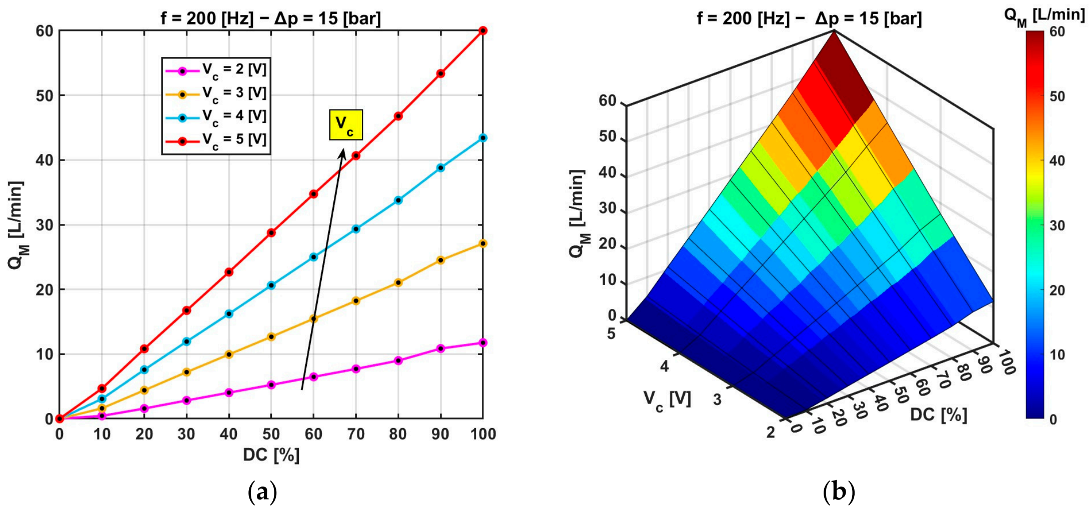

Figure 9. Open-loop predictions simulated for different values of V_c and DC (f = 200 Hz, Δp = 5 bar): (**a**) 2D plot of the Average Flow Rate; (**b**) 3D plot of the Average Flow Rate.

Figures 7–9 depict open-loop simulations conducted with an overall pressure drop across the valve set at $\Delta p = 15$ bar. The chosen pressure drop value aims to design a valve that can provide high flow rates while maintaining low pressure drops. Therefore, a pressure drop of 7.5 bar for each metering chamber (P → A and B → T) was considered appropriate for this purpose, leading to a total pressure drop of 15 bar across the valve.

Figures 10 and 11 evaluate the influence of the inlet pressure (p_p) on the average flow rate (Q_M) and the ideal average power dissipated by the valve ($P_{d,v}$). Each figure focuses on a specific quantity, with Figure 10 presenting the average flow rate and Figure 11 illustrating the ideal average power dissipated by the valve. The analysis involves varying the duty cycle (DC) while keeping the amplitude of the input control voltage constant at $V_c = 5$ V. Different values of $\Delta p = p_p - p_t$ were considered in the investigation, specifically Δp = 10 bar, Δp = 15 bar, Δp = 20 bar, Δp = 25 bar. It is worth noting that as the overall pressure drop across the valve increased, the average flow rate also increased. For example, at DC = 100% and Δp = 25 bar, the average flow rate reached its maximum value of $Q_M = 77$ L/min. However, it is important to consider the trade-off between the average flow rate and average power consumption. Since the ideal average power dissipated by the valve ($P_{d,v}$) was calculated as the product of the average flow rate (Q_M) and the pressure difference (Δp), the ideal average power consumption became significantly high. For the mentioned case of DC = 100% and Δp = 25 bar, the ideal average power dissipation amounted to $P_{d,v} = 3208$ W.

For real applications, closed-loop control is essential to ensure proper control. In this scenario, closed-loop control was simulated using a simple PI controller. The controller adjusts the duty cycle of the input control voltage, which has an amplitude of $V_c = 5$ V, based on Equation (18), to achieve the desired average flow rate (set point). The PI controller parameters, K_P and K_I, were determined using the Ziegler–Nichols method and set to 0.01125 and 3.6, respectively. The back calculation anti-windup method was employed.

In the simulated closed-loop step tests, the set point was adjusted three times, specifically from 0 to 20 L/min (Figure 12a), from 0 to 30 L/min (Figure 12b), and from 0 to 40 L/min (Figure 12c). The overall pressure difference across the valve, $\Delta p = p_p - p_t$ was set to 15 bar for these tests. The parameters specified in Tables 1 and 2 were also used in these simulations.

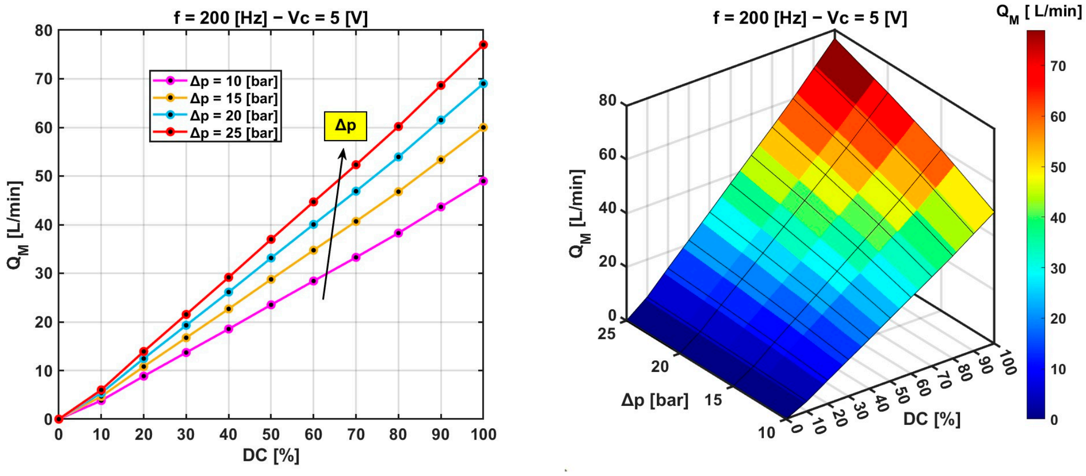

(**a**) (**b**)

Figure 10. Open-loop predictions obtained for different values of Δp and DC (f = 200 Hz, V_c = 5 V): (**a**) 2D plot of the Average Flow Rate; (**b**) 3D plot of the Average Flow Rate.

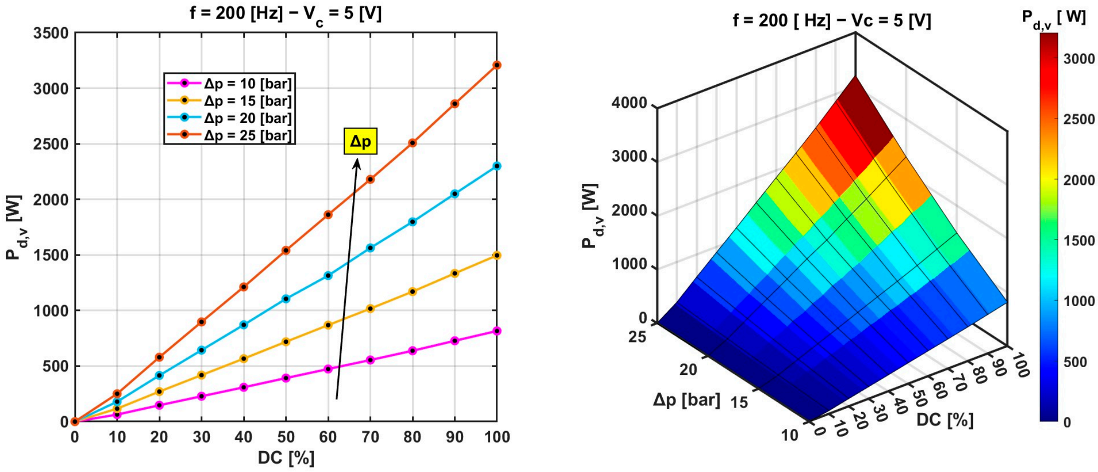

(**a**) (**b**)

Figure 11. Open-loop predictions obtained for different values of Δp and DC (f = 200 Hz, V_c = 5 V): (**a**) 2D plot of the Ideal Average Power Dissipated by the Valve; (**b**) 3D plot of the Ideal Average Power Dissipated by the Valve.

These graphs provide clear evidence of the effectiveness of the closed-loop control system. It is evident that the system efficiently reached the desired set point by making only three changes in the duty cycle of the input control voltage. Remarkably, this achievement was accomplished in less than 15 ms.

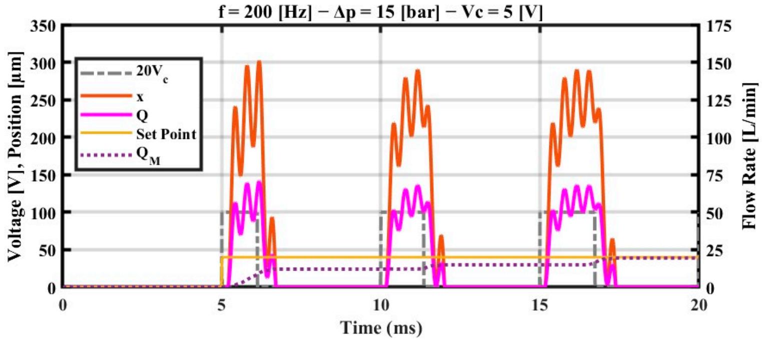

(**a**)

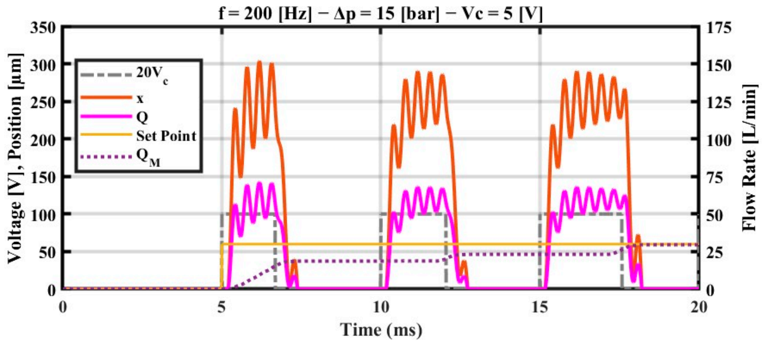

(**b**)

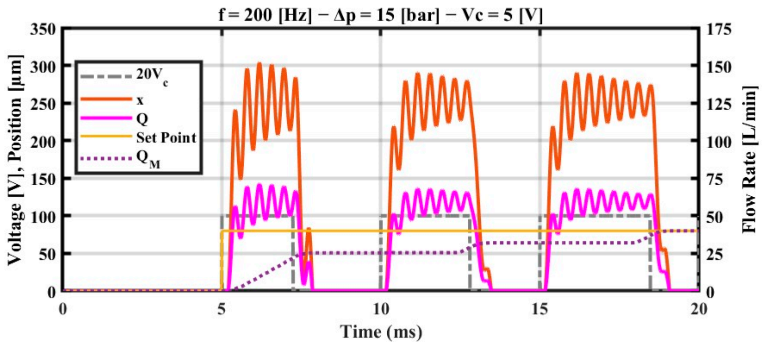

(**c**)

Figure 12. Closed-loop results (f = 200 Hz, Δp = 15 bar, V_c = 5 V): (**a**) Q_M = 20 L/min; (**b**) Q_M = 30 L/min; (**c**) Q_M = 40 L/min.

5. Conclusions

This study investigated the potential application of a commercially available ring stack actuator for the actuation of an innovative 4/2 HFSV (High-Frequency Switching Digital Hydraulic Valve). By harnessing the benefits provided by these piezo actuators, such as their rapid response and lightweight characteristics, the demanding requirements of such digital hydraulic valves have been successfully met.

The effectiveness of the designed 4/2 HFSV architecture was assessed by applying well-established equations within a Simulink environment. The hysteresis of the ring stack actuator was precisely simulated through the utilization of the Bouc–Wen model, and its accuracy was verified through a comparison with experimental data, which showed a percentage error of less than 15% in both the ascending and descending branches.

The analysis presented numerical results obtained from an open-loop control system, followed by discussions of the results obtained in closed-loop control. The simulations, along with the analysis of the ring stack actuator's characteristics, revealed both the advantages and disadvantages of the proposed valve's architecture.

In terms of positive aspects, the proposed valve design stands out for its simplicity, as the ring stack directly controls the opening and closing of poppets with the application or removal of the input pulse digital signal. The simulations demonstrated that the actuation force provided by the piezoelectric actuator was capable of overcoming the opposing forces and ensuring a rapid response, enabling the valve to reach the open position in less than 1 ms. Additionally, the hysteresis of the ring stack actuator wasn't a significant problem, as the stored force in the additional spring was ample to ensure the poppets closed the valve when the input pulse digital signal was removed.

In the simulated open-loop tests, it was observed that increasing the amplitudes and duty cycles of the input pulse signal, as well as the pressure drops across the valve, led to higher average flow rates and average power consumption. This finding highlighted the need to find a trade-off between the average flow rate and the average power dissipation. The optimal trade-off was found to be a duty cycle of 100%, an amplitude of 5 V for the input pulse digital signal, and an overall pressure drop of 15 bar across the valve. This resulted in an average flow rate of 60 L/min and an average power dissipation of only 1500 W, meeting the stringent requirements of HFSVs.

The closed-loop step tests were performed to evaluate the effectiveness of the control system. The code was configured with three different set points for the desired average flow rate, specifically 20 L/min, 30 L/min, and 40 L/min. The numerical results demonstrated that the control system successfully achieved the desired average flow rate by adjusting the duty cycle of the input control voltage only three times, all within a duration of less than 15 ms.

In terms of negative aspects, the simulations showed that due to the high switching frequency of the input pulse digital signal and the low value of the poppets' damping factor (e.g., 60 N/ms), the mass of the moving parts must be sufficiently small (e.g., 100 g) to limit the oscillations in the poppet positions and the instantaneous flow rate. Additionally, the high cost and large size of piezoelectric actuators, along with the need for a high-performance amplifier, pose challenges for the proposed valve architecture. Nevertheless, the potential future mass production of these actuators might present a promising resolution to mitigate their high cost.

Author Contributions: Conceptualization, P.T., F.S., E.D. and R.A.; Methodology, P.T., F.S., E.D. and R.A.; Software, P.T., F.S., E.D. and R.A.; Validation, P.T., F.S., E.D. and R.A.; Formal analysis, P.T., F.S., E.D. and R.A.; Investigation, P.T., F.S., E.D. and R.A.; Resources, P.T., F.S., E.D. and R.A.; Data curation, P.T., F.S., E.D. and R.A.; Writing—original draft, P.T., F.S., E.D. and R.A.; Writing—review & editing, P.T., F.S., E.D. and R.A.; Visualization, P.T., F.S., E.D. and R.A.; Supervision, P.T., F.S., E.D. and R.A.; Project administration, P.T., F.S., E.D. and R.A. All authors have read and agreed to the published version of the manuscript.

Funding: This research received no external funding.

Data Availability Statement: The simulation code is available at: https://drive.google.com/drive/folders/14EuhckFev2mExXWd9rN1ZGPt5PCb6DyD?hl=it (accessed on 5 June 2023).

Conflicts of Interest: The authors declare no conflict of interest.

References

1. Tamburrano, P.; Plummer, A.R.; Distaso, E.; Amirante, R. A review of electro-hydraulic servovalve research and development. *Int. J. Fluid. Power* **2019**, *20*, 53–98. [CrossRef]
2. Tamburrano, P.; Plummer, A.R.; Distaso, E.; Amirante, R. A review of direct drive proportional electrohydraulic spool valves: Industrial state-of-the-art and research advancements. *J. Dyn. Syst. Meas. Control Trans. ASME* **2019**, *141*, 020801. [CrossRef]
3. Zhu, Q.; Huang, D.; Yu, B.; Ba, K.; Kong, X.; Wang, S. An improved method combined SMC and MLESO for impedance control of legged robots' electro-hydraulic servo system. *ISA Trans.* **2022**, *130*, 598–609. [CrossRef] [PubMed]
4. Chen, X.; Jiao, Z.; Liu, X.; Li, X.; Qi, P.; Shang, Y. Experimental validation of a practical nonlinear control method for hydraulic flight motion simulator. *J. Frankl. Inst.* **2022**, *359*, 2405–2423. [CrossRef]
5. Sciatti, F.; Tamburrano, P.; De Palma, P.; Distaso, E.; Amirante, R. Detailed simulations of an aircraft fuel system by means of Simulink. *J. Phys. Conf. Ser.* **2022**, *2385*, 012033. [CrossRef]

6. Padovani, D.; Fresia, P.; Rundo, M.; Altare, G. Downsizing the electric machines of energy-efficient electro-hydraulic drives for mobile hydraulics. *J. Phys. Conf. Ser.* **2022**, *2385*, 012028. [CrossRef]
7. Sun, X.; Liu, S.; Bao, J.; Li, J.; Liu, Z. A performance prediction method for a high-precision servo valve supported by digital twin assembly-commissioning. *Machines* **2021**, *10*, 11. [CrossRef]
8. Gao, B.; Zhang, W.; Zheng, L.; Zhao, H. Research on High-Precision Position Control of Valve-Controlled Cylinders Based on Variable Structure Control. *Machines* **2023**, *11*, 623. [CrossRef]
9. Heinken, H.; Ulrich, S.; Bruns, R.; Schneider, S. High-response electrorheological servo valve. *J. Intell. Mater. Syst. Struct.* **2020**, *31*, 297–307. [CrossRef]
10. Tamburrano, P.; Sciatti, F.; Plummer, A.R.; Distaso, E.; De Palma, P.; Amirante, R. A review of novel architectures of servovalves driven by piezoelectric actuators. *Energy* **2021**, *14*, 4858. [CrossRef]
11. Liang, N.; Yuan, Z.; Zhang, F. Oil Particle-Induced Erosion Wear on the Deflector Jet Servo Valve Prestage. *Aerospace* **2023**, *10*, 67. [CrossRef]
12. Alemdaroglu, U.; Guler, Z.; Sevim, S.; Dalkiran, F. Energy efficiency by reducing throttling losses in hydraulic systems. *J. Mechatron. Artif. Intell. Eng.* **2023**, *4*, 1–7. [CrossRef]
13. Mahato, A.C.; Ghoshal, S.K. Energy-saving strategies on power hydraulic system: An overview. *Proc. Inst. Mech. Eng. Part. I J. Syst. Control Eng.* **2021**, *235*, 147–169. [CrossRef]
14. Tamburrano, P.; De Palma, P.; Plummer, A.R.; Distaso, E.; Sciatti, F.; Amirante, R. Simulation of a high frequency on/off valve actuated by a piezo-ring stack for digital hydraulics. In *E3S Web of Conferences*; EDP Sciences: Les Ulis, France, 2021; Volume 312, p. 05008.
15. Karpenko, M.; Stosiak, M.; Šukevičius, Š.; Skačkauskas, P.; Urbanowicz, K.; Deptuła, A. Hydrodynamic Processes in Angular Fitting Connections of a Transport Machine's Hydraulic Drive. *Machines* **2023**, *11*, 355. [CrossRef]
16. Laamanen, M.S.A.; Vilenius, M. Is it time for digital hydraulics. In Proceedings of the Eighth Scandinavian International Conference on Fluid Power, Tampere, Finland, 7–9 May 2003.
17. Scheidl, R.; Linjama, M.; Schmidt, S. Is the future of fluid power digital? *Proc. Inst. Mech. Eng. Part. I J. Syst. Control Eng.* **2012**, *226*, 721–723. [CrossRef]
18. Achten, P.; Linjama, M.; Scheidl, R.; Schmidt, S. Discussion: Is the future of fluid power digital? *Proc. Inst. Mech. Eng. Part. I J. Syst. Control Eng.* **2012**, *226*, 724–727. [CrossRef]
19. Zhang, Q.; Kong, X.; Yu, B.; Ba, K.; Jin, Z.; Kang, Y. Review and development trend of digital hydraulic technology. *Appl. Sci.* **2020**, *10*, 579. [CrossRef]
20. Jiao, Z.; Zhang, H.; Shang, Y.; Liu, X.; Wu, S. A power-by-wire aircraft brake system based on high-speed on-off valves. *Aerosp. Sci. Technol.* **2020**, *106*, 106177. [CrossRef]
21. Jing, Y.A.O.; Pei, W.; Zhaosheng, D.; Jiang, D.; Tong, S.H.A. A novel architecture of electro-hydrostatic actuator with digital distribution. *Chin. J. Aeronaut.* **2021**, *34*, 224–238.
22. Gao, Q.; Zhu, Y.; Liu, J. Dynamics modelling and control of a novel fuel metering valve actuated by two binary-coded digital valve arrays. *Machines* **2022**, *10*, 55. [CrossRef]
23. Gao, Q.; Zhu, Y.; Wu, C.; Jiang, Y. Development of a novel two-stage proportional valve with a pilot digital flow distribution. *Front. Mech. Eng.* **2021**, *16*, 420–434.
24. Zhong, Q.; Bao, H.; Li, Y.; Hong, H.; Zhang, B.; Yang, H. Investigation into the independent metering control performance of a twin spools valve with switching technology-controlled pilot stage. *Chin. J. Mech. Eng.* **2021**, *34*, 91.
25. Yang, M. Study on the Digital hydraulic driving system of the belt conveyor. *Machines* **2022**, *10*, 417.
26. Hansen, A.H.; Asmussen, M.F.; Bech, M.M. Hardware-in-the-Loop validation of model predictive control of a discrete fluid power power Take-Off system for wave energy converters. *Energy* **2019**, *12*, 3668. [CrossRef]
27. Brandstetter, R.; Deubel, T.; Scheidl, R.; Winkler, B.; Zeman, K. Digital hydraulics and 'Industrie 4.0'. *Proc. Inst. Mech. Eng. Part. I J. Syst. Control Eng.* **2017**, *231*, 82–93.
28. Wang, H.; Chen, Z.; Huang, J.; Quan, L.; Zhao, B. Development of high-speed on–off valves and their applications. *Chin. J. Mech. Eng.* **2022**, *35*, 67.
29. Zhong, Q.; Zhang, B.; Yang, H.-Y.; Ma, J.-E.; Fung, R.-F. Performance analysis of a high-speed on/off valve based on an intelligent pulse-width modulation control. *Adv. Mech. Eng.* **2017**, *9*, 1687814017733247.
30. Gao, Q.; Wang, J.; Zhu, Y.; Wang, J.; Wang, J. Research Status and Prospects of Control Strategies for High Speed on/off Valves. *Processes* **2023**, *11*, 160.
31. Linjama, M. Digital Fluid Power-State of the Art. In Proceedings of the Twelfth Scandinavian International Conference on Fluid Power, Tampere, Finland, 18–20 May 2011.
32. Zhong, B.; Liao, Z.; Zhang, X.; Jin, Z.; Sun, L. Modeling of Rapid Response Characteristics of Piezoelectric Actuators for Ultra-Precision Machining. *Materials* **2023**, *16*, 2272.
33. Yokota, S.; Hiramoto, K.; Akutsu, K. An ultra fast-acting electro-hydraulic digital valve and high-speed electro-hydraulic servo valves using multilayered PZT elements. In *Proceedings of the JFPS International Symposium on Fluid Power*; The Japan Fluid Power System Society: Tokyo, Japan, 1993; pp. 121–130.
34. Yokota, S.; Akutu, K. A fast-acting electro-hydraulic digital transducer: A poppet-type on-off valve using a multilayered piezoelectric device. *JSME Int. J. Ser. 2 Fluids Eng. Heat. Transf. Power Combust. Thermophys. Prop.* **1991**, *34*, 489–495.

35. Yamada, H.; Wennmacher, G.; Muto, T.; Suematsu, Y. Development of a high-speed on/off digital valve for hydraulic control systems using a multilayered PZT actuator. *Int. J. Fluid. Power* **2000**, *1*, 5–10.
36. Ouyang, X.; Yang, H.; Jiang, H.; Xu, B. Simulation of the piezoelectric high-speed on/off valve. *Chin. Sci. Bull.* **2008**, *53*, 2706–2711. [CrossRef]
37. Yu, J.; Jiao, Z.; Wu, S. Design and Simulation of high-flow high-speed on-off valve driven by piezoelectric. In Proceedings of the 2019 IEEE 8th International Conference on Fluid Power and Mechatronics (FPM), Wuhan, China, 10–13 April 2019; IEEE: Piscataway, NJ, USA; pp. 617–623.
38. Le Letty, R.; Sosnicki, O.; Barillot, F.; Claeysssen, F. Actuators in Adaptronics: Piezoelectric Actuators. In Proceedings of the II ECCOMAS Thematic Conference on Smart Structures and Materials, Lisbon, Portugal, 18–21 July 2005.
39. Noliac. Available online: http://www.noliac.com/products/actuators/ring-stacks/show/nac2125-hxx/ (accessed on 22 September 2023).
40. Fouaidy, M.; Saki, M.; Hammoudi, N.; Simonet, L. *Electromechanical Characterization of Piezoelectric Actuators Subjected to a Variable Pre-Loading Force at Cryogenic Temperature*; IPN: Mexico City, Mexico, 2007.
41. Yong, Y.K. Preloading piezoelectric stack actuators in high-speed nanopositioning systems. *Front. Mech. Eng.* **2016**, *2*, 8. [CrossRef]
42. Engine Parts Technical Supplements. Available online: https://www.dura-bondbearing.com/wp-content/uploads/2018/06/valve-seat-tech-guide.pdf (accessed on 22 September 2023).
43. The MathWorks Inc. *Matlab & Simulink SimscapeTM User's Guide R2023a*; The MathWorks Inc.: Natick, MA, USA, 2023.
44. Tamburrano, P.; Distaso, E.; Plummer, A.R.; Sciatti, F.; De Palma, P.; Amirante, R. Direct drive servovalves actuated by amplified piezo-stacks: Assessment through a detailed numerical analysis. *Actuators* **2021**, *10*, 156. [CrossRef]
45. Fan, Y.L.; Lei, Y.; Zhang, J.W.; Wang, J.; Li, Z. Flow Force of Pressure Independent Control Valve with Different Valve Core Structural. *J. Phys. Conf. Ser.* **2020**, *1634*, 12149. [CrossRef]
46. Li, R.; Sun, Y.; Wu, X.; Zhang, P.; Li, D.; Lin, J.; Xia, Y.; Sun, Q. Review of the Research on and Optimization of the Flow Force of Hydraulic Spool Valves. *Processes* **2023**, *11*, 2183. [CrossRef]
47. Manring, N.D.; Fales, R.C.; Manring, N.D.; Fales, R.C. *Hydraulic Control Systems*; John Wiley & Sons: Hoboken, NJ, USA, 2019.